CrossMark

ORIGINAL PAPER

Optimizing ductility and fracture of amorphous metal thin films on polyimide using multilayers

Hai T. Tran · Hesham Mraied · Sina Izadi · Alex A. Volinsky · Wenjun Cai

Abstract Aluminum–manganese (Al–Mn) thin films with manganese concentration up to 20.5 at.% were deposited on polyimide (PI) substrates. A variety of phases, including supersaturated fcc (5.2 at.% Mn), duplex fcc and amorphous (11.5 at.% Mn), and completely amorphous phase (20.5 at.% Mn) were obtained by adjusting alloying concentration in the film. Tensile deformation and subsequent fracture of strained Al–Mn films on PI were investigated experimentally and by finite element simulations. Compared with crystalline and dual phase counterparts, amorphous thin film exhibits the highest fracture stress and fracture toughness, but limited elongation. Based on the fracture mechanism model, a multilayer scheme was adopted to optimize the ductility and the fracture properties of the amorphous film/PI system. It was found that by sandwiching the amorphous film (20.5 at.% Mn) between two ductile Cu layers, the elongation can be improved by more than ten times, and the interfacial fracture toughness by more than twenty times. This design provides important guidelines to obtain opti-

H. T. Tran · H. Mraied · S. Izadi · A. A. Volinsky ·
W. Cai (✉)
Department of Mechanical Engineering, University of
South Florida, 4202 E. Fowler Ave ENB118,
Tampa, FL 33620, USA
e-mail: caiw@usf.edu

H. T. Tran
Department of Mechanical Engineering, University of Transport
and Communications, Cau Giay, Hanoi, Vietnam

mized mechanical properties of future flexible electronics devices.

1 Introduction

Flexible electronics has gained great interest lately due to potential applications as wearable electronic devices (Wagner et al. 2004), sensor skins (Lumelsky et al. 2001), electronic textiles (Bonderover and Wagner 2004), and flexible solar cells (Brabec 2004), etc. Ductility mismatch between the metallic interconnect thin films and the flexible polymer substrate has often led to limited stretchability and thus hindering reliable performance of the whole system. Various strategies have been adopted to improve the stretchability of the metal film coated on polymer, mostly focusing on crystalline thin films, such as Cu and Cr, etc. Metallic film rupture strain has been found to be highly sensitive to film adhesion to the substrate. Improved film/substrate adhesion delays interfacial decohesion and retards strain localization, such as necking or shear band formation in the film (George et al. 2005; Xiang et al. 2005). Annealing at relatively low temperatures also improves the strechability and fracture toughness of crystalline thin films by grain growth and other related phenomena (Lu et al. 2009). Compared with

crystalline metallic films, various amorphous alloys stand out to be good candidates as functional materials due to their good metallic bonding ability (Chu et al. 2009; Inoue 2001; Wang 2009), excellent mechanical, corrosion (Chu et al. 2010; Moffat et al. 1993), and magnetic properties (McHenry et al. 1999; Phan and Peng 2008). However, amorphous alloys are intrinsically brittle. When stretched, the glassy film cannot sustain the required co-deformation with the substrate. Such considerations have motivated the authors to improve the mechanical properties (focusing on fracture toughness, interfacial fracture toughness and elongation) of amorphous metal films coated on polymer substrates.

Most amorphous alloys are quasi-brittle due to the lack of strain hardening mechanisms or any intrinsic crack propagation barriers, such as grain boundaries or secondary phase boundaries. Therefore, their limited ductility and low fracture toughness often lead to high sensitivity to structural variables, such as surface roughness, making them unreliable for the widespread use (Schuh et al. 2007). One solution for this issue is adding crystalline metal layer(s) to create a hierarchical multilayered structure (Misra et al. 2005; Wang and Anderson 2005; Zhang et al. 2014). The ductile crystalline layer will mitigate the catastrophic shear bands propagation of the amorphous layers and localize crack propagation. Despite current progress, there have been very limited attempts to characterize the fracture behavior of amorphous alloys, especially under tensile loading conditions. In this work, Cu was chosen as the crystalline buffer layer to the amorphous film due to its relatively high elongation and tensile strength. It was proposed that if the strength of the well-adhered crystalline layer is similar or higher than that of the amorphous counterpart, the amorphous layer will be constrained by the crystalline one, making the whole multilayered film fail at a larger strain (Chen et al. 2011b; Li et al. 2007; Nieh et al. 1999). In this work, crystallinity of the Al thin films was tuned by varying Mn concentration in the alloy (Ruan and Schuh 2009). Increasing Mn% from 5.2 to 20.5 at.% leads to a phase transformation from supersaturated fcc phase with moderate ductility to brittle amorphous phase. Thin film microstructure and composition were characterized using scanning electron microscopy (SEM), energy dispersive spectra (EDS), transmission electron microscopy (TEM) and selected area diffraction (SAD). Tensile tests of metal coated polyimide (PI)

were performed and the strains were measured using digital image correlation (DIC) method. It was found that the amorphous Al-20.5 at.% Mn exhibits the highest fracture stress and fracture toughness, but lowest ductility. Further improvement of fracture toughness, interfacial fracture toughness and elongation of the amorphous alloy/PI system was achieved by adopting bilayered and trilayered structure using ultrathin Cu buffer layers. Finally, the failure mechanisms of the layered films were modeled using finite element analysis (FEA).

2 Experimental procedure

Al–Mn thin films were magnetron sputtered on $7.6\,\mu$m thick PI foils (Kapton HN by DuPont). Prior to film deposition, the PI substrates were ultrasonically cleaned with acetone and ethanol. All depositions were performed using the CRC-100 sputtering system with 70 W RF power at a base pressure of 1×10^{-6} Torr. The nominal target-substrate distance was 60 mm and the deposition rate was about 0.11 nm/s. Six sets of samples were prepared, as listed in Table 1. The total thickness of metallic films on all samples was kept at about 1.2 μm to minimize the film thickness effect on fracture strain (Cordill et al. 2010). Samples M5 (Al-5.2 at.% Mn), M11 (Al-11.5 at.% Mn) and M20 (Al-20.5 at.% Mn) are 1.2 μm thick monolithic films on PI substrate. Samples B1 and B2 are bilayered films with 50 and 100 nm Cu buffer layer between the PI substrate and the Al–Mn film, respectively, with the total film thickness (i.e. thickness of both the Cu and Al–Mn layer) of 1.2 μm. Sample S is a trilayered structure on the PI substrate, with two Cu layers (100 nm) sandwiching the Al-20.5 at.% Mn layer (1 μm). After film deposition, coated PI exhibits negligible curvature change, thus the residual stress in the film is neglected in this study. This is consistent with extensive previous reports showing that the highly compressive residual stress in thin films increases (or the absolute value decreases) rapidly with increasing film thickness and becomes close to zero at layer thicknesses greater than 500 nm (Frank et al. 2011).

Surface morphology and chemical composition of as-deposited samples were characterized using scanning electron microscopy (Hitachi SU-70) and energy dispersive spectrometer (EDAX-Phoenix). TEM samples were prepared by directly sputtering Al–Mn alloys

Table 1 Composition and mechanical properties of monolithic (M5, M11, and M20), bilayer (B1 and B2), and trilayer (S) Al–Mn thin films deposited on PI substrates

Sample ID	Composition	h_{Cu} (nm)	ε_c (%)	σ_f (MPa)	ν	E (GPa)	K_{Ic} (MPa m$^{1/2}$)	Crit. J-int (J/m^2)
M5	Al–5.2 at.% Mn	–	0.63 ± 0.06	199.1 ± 8.6	0.34	39.4 ± 7.3	0.58	–
M11	Al–11.5 at.% Mn	–	0.57 ± 0.08	221.1 ± 13.4	0.33	62.3 ± 5.9	0.78	–
M20	Al–20.5 at.% Mn	–	0.46 ± 0.01	321.7 ± 22.7	0.32	103.6 ± 2.9	1.38	0.34
B1	Cu|Al−20.5 at.% Mn	50	6.24 ± 1.14	220.8 ± 11.9	0.32	67.8 ± 2.6	0.79	8.55
B2	Cu|Al−20.5 at.% Mn	100	2.32 ± 0.24	324.3 ± 15.9	0.32	90.7 ± 11.6	1.21	2.19
S	Cu|Al−20.5 at.% Mn|Cu	100	5.67 ± 0.69	284.1 ± 5.6	0.32	94.9 ± 10.8	1.13	8.13

h_{Cu} is the thickness of the Cu layer(s) in the samples. The critical strain (ε_c), fracture stress (σ_f) and elastic modulus (E) were measured from the stress-strain curves of uniaxial tensile tests. The Poisson's ratio (ν) was estimated using the rule of mixtures from pure Al and Mn (Cardarelli 2008). Critical J-integrals of the film/substrate interface (interfacial fracture toughness) of sample M20, B1, B2, and S were calculated by FEA at their corresponding critical strains

on continuous carbon film grids for 15 min to reach a sample thickness of ∼150 nm. Bright-field (BF), dark-field (DF) imaging, and SAD analysis were performed using a Tecani F20 TEM operated at 200 kV with a field emission gun.

Uniaxial tensile tests (DTS, National Instruments) were carried out at a constant strain rate of 4×10^{-4} s^{-1} at room temperature. Rectangular samples with 4×20 mm^2 gauge area were used. All results reported were obtained by averaging from at least four separate tests. Electrical resistance of the samples was recorded using Tektronix 4050 multimeter during the test. The critical strain ε_c, i.e. the macroscopic strain which characterizes the microcrack formation (as opposed to rupture), was obtained by using electrical resistance change method (Niu et al. 2007). Figure 1 shows a typical evolution of electrical resistance change during a tensile test, where ε_c is defined at the point where the electrical resistance deviated from the ideal curve (Lu et al. 2007; Niu et al. 2007). The force of the film (F_{film}) at a certain displacement was estimated as $F_{film} = F_{total} - F_{substrate}$ (Macionczyk and Brückner 1999; Pei et al. 2011) (neglecting the force required to break the native oxide layer on the metallic film), where F_{total} and $F_{substrate}$ are the tensile loads of the thin film-coated and uncoated PI specimen at the same displacement, respectively. The tensile stress of the film was then calculated as $\sigma = F_{film}/wt$, where w and t are the width and the thickness of the film, respectively. Strain was measured during tensile tests using digital image correlation method by tracing the makers (sprayed ink speckles) displacements using a high definition camera (1920 × 1080 pixels, 30 fps) (Bing Pan et al. 2009). The strain was then calculated from
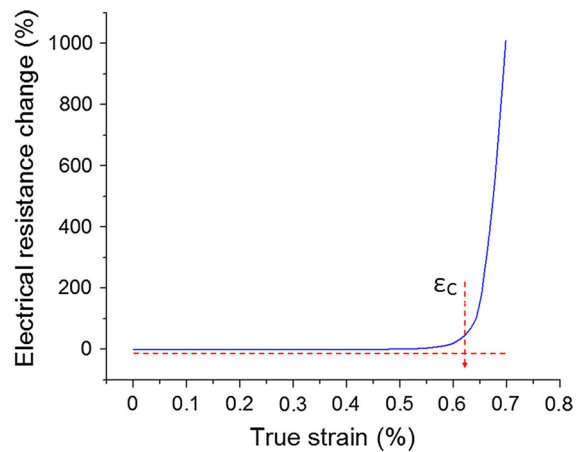

Fig. 1 Evolution of electrical resistance change (defined as $(R–R_0)/R_0$, where R_0 is the initial electrical resistance of the film) of a monolithic Al-5.2 at.%Mn (sample M5) as a function of strain

the recorded images using a Matlab routine developed by Eberl et al. (2010).

3 Microstructure of as-deposited Al–Mn

Microstructure of as-deposited monolithic Al–Mn was studied by TEM and SAD, as shown in Fig. 2. Increasing Mn% in the alloy leads to a phase transition from a supersaturated fcc structure to a completely amorphous phase, similar to electrodeposited Al–Mn (Ruan and Schuh 2009). At 5.2 at.% Mn, Fig. 2a shows that sample M5 contains a single fcc phase (lattice constant $a = 4.036$ Å) with an average grain size <d> of ∼15 nm. At the intermediate Mn concentration of 11.5 at.%, M11 contains a complex dual phase structure, where
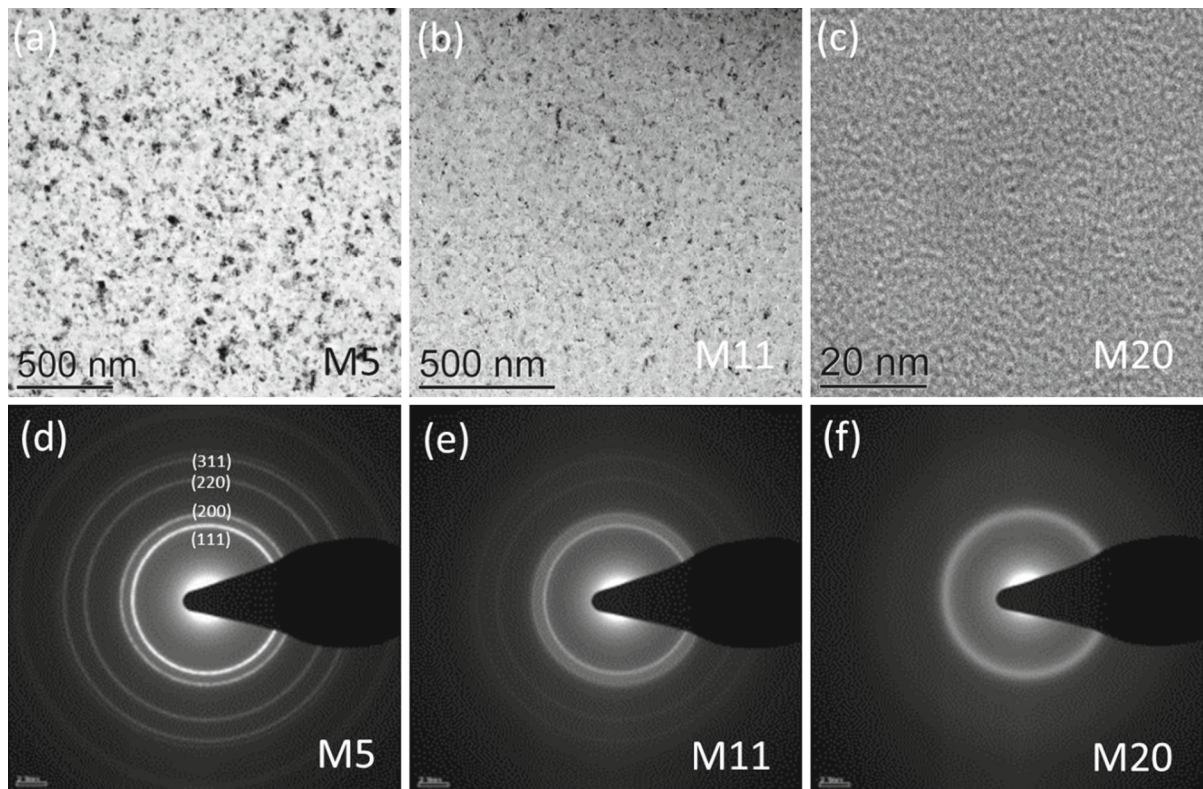
Fig. 2 a–c TEM images and **d, e** corresponding SAD patterns of as-deposited monolithic Al–Mn films with various Mn % as defined in Table 1

nanocrystalline fcc (a = 4.035 Å and $<d> = 12$ nm) and amorphous phases coexist. Further increasing Mn concentration to 20.5 at.% leads to the formation of a completely amorphous microstructure of M20, as confirmed by the diffuse halo in the SAD pattern (Fig. 2f).

4 Tensile behaviors of monolithic and multilayered samples

Typical true stress-strain curves of the monolithic and multilayer samples are shown in Fig. 3. The arrows indicate the critical strains (ε_c). Table 1 lists the mechanical properties obtained from the stress-strain curves, including elastic modulus (E), fracture stress (σ_f, i.e. the film stress at its critical strain), critical strain (ε_c), and fracture toughness (K_{Ic}). The mode I stress intensity factor K_{Ic} (fracture toughness) was calculated from the energy release rate G as (Freund and Suresh 2003):

$$K_{Ic} = \sqrt{\frac{EG}{1 - \nu^2}}, \tag{1}$$

where E and ν are the elastic modulus and the Poisson's ratio of the film, respectively. The steady-state energy release rate G was calculated as (Beuth Jr 1992):

$$G = \frac{\pi \sigma_f^2 h_T}{2E} \left(1 - \nu^2\right) g\left(\alpha, \beta\right), \tag{2}$$

where h_T is the total thickness of the film ($\sim$1.2 µm), $g\left(\alpha, \beta\right)$ is a dimensionless quantity determined by the elastic mismatch between the film and the substrate, and α and β are the two Dundurs' parameters defined as:

$$\alpha = \frac{\bar{E}_1 - \bar{E}_2}{\bar{E}_1 + \bar{E}_2}, \text{ and } \beta = \frac{\mu_1 \left(1 - 2\nu_2\right) - \mu_2 \left(1 - 2\nu_1\right)}{2\mu_1 \left(1 - \nu_2\right) + 2\mu_2 \left(1 - \nu_1\right)}, \tag{3}$$

where $\bar{E} = E / \left(1 - \nu^2\right)$ is the plane strain tensile modulus and μ is the shear modulus. The subscripts 1 and 2 refer to the film and the PI, respectively. In this work, α ranges from 0.87 to 0.95, $\beta \approx \alpha/4$ and $g\left(\alpha, \beta\right)$ are linear interpolation values obtained from reference (Beuth Jr 1992). It should be noted the energy release rate calculated from Eq. (2) considers a single channeling crack

in a thin film on a semi-infinite substrate, while the effect of crack spacing on G is neglected. For deformed ductile thin films such as Cu on compliant substrate, parallel channel cracks are often observed perpendicular to the loading direction. It was shown that the energy release rate of such thin films increases with crack spacing for a given film (and substrate) thickness and eventually reaches a maximum (saturated) value that corresponds to the case with a single isolated crack (Huang et al. 2003). However, as will be shown later in Sect. 4.2, the deformed amorphous Al–Mn (M20) thin film studied here do not exhibit the typical parallel channel cracks, but rather extensive shear bands inclined or perpendicular to the loading direction. For samples with Cu buffer layers such as B1, B2 and S, parallel cracks were indeed observed (Fig. 5b–d), with crack spacing between ∼50 and 100 μm and crack spacing to film thickness ratio around ∼ 42–83. In such cases, the energy release rate is approaching the saturated value as calculated here. Hence, considering the behavior of both monolithic (M20) and layered samples (B1, B2, and S), we neglect the effect of crack spacing and adopt Eq. (2) to calculate G for simplicity, while it should be noted that such calculations correspond to an upper limit of the steady state energy release rate for some samples.

Representative true stress-strain curves of all samples are shown in Fig. 3. For all monolithic samples, the stress reaches a maximum at the critical strain, followed by a stress relaxation due to crack and/or shear band formation. In addition, all mechanical properties, including σ_f, E, and K_{Ic} were found to increase with Mn %, with M20 exhibiting the highest values of all, as shown in Fig. 4 and Table 1. However, at the highest Mn concentration (20.5 at.%), the amorphous nature of M20 renders a very low tensile ductility (∼0.46%). This is not surprising given that amorphous alloys lack sufficient intrinsic mechanisms to hinder crack propagation or strain hardening (Schuh et al. 2007). Figure 5a shows a typical SEM image of the surface of M20 at the critical strain. Extensive shear bands, either inclined at an angle of ∼ 45° or perpendicular to the loading direction can be seen (indicated by white arrows), which contribute to the failure of an amorphous material (Schuh et al. 2007).

The critical strains remain very low (less than 0.65%) for all monolithic samples regardless of their crystallinity, similar to the behavior of brittle thin films such as Cr (<1%) (Cordill et al. 2010) and Ta (0.6%)
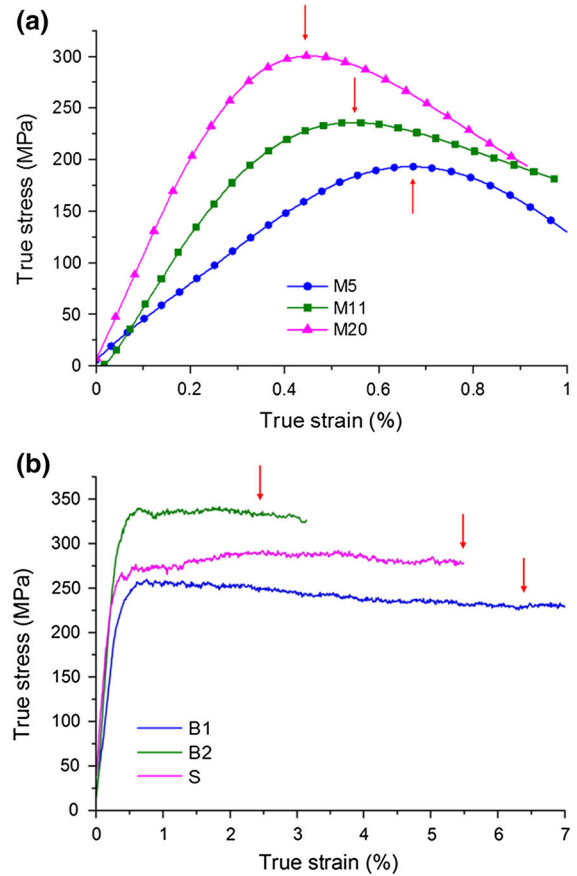
Fig. 3 **a** Representative true stress-strain curves of M5, M11 and M20 and **b** B1, B2 and S samples. The arrows indicate the critical strains ε_c

(Frank et al. 2009) on PI. To improve the film/substrate adhesion and stretchability of the system, bilayered (B1 and B2) and trilayered (S) samples were designed via extrinsic toughening mechanisms (Hofmann et al. 2008; Ritchie 2011). Figure 3b shows the true stress-strain curves of all layered samples (B1, B2, and S). It can be seen that while ε_c occurred in the elastic domain in all monolithic samples (Fig. 3a), it always occurred after extensive plastic deformation in the multilayered samples. Figure 4a shows that the bilayer scheme (B1) can enhance the elongation of M20 by more than ten times (from 0.46 to 6.24%). However, at the same time, the fracture toughness decreased from 1.38 to 0.79 MPa m$^{1/2}$. In contrast to B1, B2 samples maintained high fracture toughness of M20 and moderate improvement of critical strain (from 0.46 to 2.32%). Finally, the trilayer sample S turned out to be the optimized solution, which exhibits a combination of high ductility (5.67%), fracture stress (∼ 284 MPa) and fracture
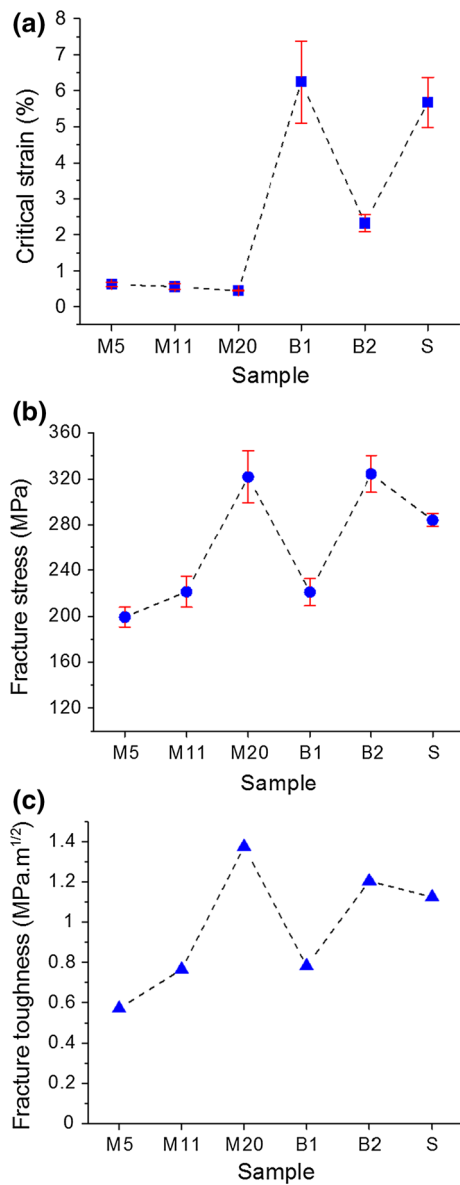
Fig. 4 **a** Critical strain, **b** fracture stress, and **c** fracture toughness of all monolithic, bilayer, and trilayer samples. *Error bars* represent standard deviation obtained from at least four separate tests

toughness (1.13 MPa m$^{1/2}$). The following discussions justify these experimental observations.

4.1 Fracture mechanisms at the brittle/ductile interface in the multilayered samples

In a ductile/brittle layered structure, crack often initiates in the brittle layer and then travels to the duc-

tile/brittle interface (Wu et al. 2014). As long as the thickness (*h*) of the ductile layer (e.g. Cu in this work) is much larger than its Burgers vector, emitted dislocations will move away from the crack tip under tensile loading (Hsia et al. 1994). In the ductile layer, emitted dislocations will blunt the crack tip and therefore reduce the tensile stress at the crack tip. Hence, the crack propagation process is suppressed, since the crack tip stress is unable to reach the cohesive tensile strength of the interface (Hsia et al. 1994). Moreover, if the strength of the ductile material is increased, its fracture toughness will be increased because of the plastic deformation during crack propagation (Was and Foecke 1996). Therefore, adding a ductile Cu layer has the potential to improve the ductility as well as the fracture toughness of the amorphous Al–Mn/PI structure. However, the dislocations emitted in the ductile layer are also confined by the brittle layer. These dislocations pile up at the interface, generating additional stress at the crack tip, which hinders further dislocation emission and blunting process at the crack tip (Anderson and Li 1993). Gradually, the tensile stress at the blunted crack tip reaches a critical strength resulting in fracture. Therefore, the fracture toughness of the film depends on the number of dislocations emitted, which in turn depends on the thickness of the ductile layer (Hsia et al. 1994).

What is the appropriate ductile layer thickness that should be added to the amorphous M20 sample to optimize its ductility and fracture toughness? We approach this problem by evaluating the constraining effect of the ductile layer on the fracture behavior of a composite material consisting of alternating ductile and brittle layer(s). In a ductile metallic layer with a crack, the plastic zone size at the crack tip can be estimated as (Hsia et al. 1994):

$$r_p = \frac{1}{2\pi}\left(\frac{K_{I_c}}{\sigma_Y}\right)^2, \tag{4}$$

where K_{I_c} is the fracture toughness and σ_Y is the yield strength of the material. When the layer thickness (*h*) of the ductile phase is large, the plastic zone size is on the order of millimeters or even centimeters, similar to its bulk counterpart. However, in thin films with *h* ranging from a few micrometer to ∼10 nm, the plastic zone is confined ($h < r_p$), resulting in a reduced fracture toughness (Hsia et al. 1994; Varias et al. 1991). In this case, dislocation activities in ductile thin film (Cu layer) no longer obey the continuum plasticity theory.

The discrete dislocations interact with the crack tip and the interfaces, while the interfaces serve as barriers preventing dislocations from crossing over into the brittle layer. Because of this dislocation confinement, fracture toughness increases with the ductile layer thickness (Hsia et al. 1994). For example, Wu et al. (2014) showed that in Cu/Mo multilayers coated on PI, the adhesion energy remains low when the thickness of the ductile Cu layer (h_{Cu}) is below ~ 25 nm, but increases rapidly with h_{Cu} afterwards. Zhang (2011) studied the effect of layer thickness on the fracture behavior of Cu/Nb and Cu/Zr multilayers coated on PI. They found that the fracture mode of the mutlilayers is controlled by the constraining effect of the Cu layer and the fracture toughness increases with h_{Cu} and reaches a steady-state at $h_{Cu} > 20-30$ nm. When h_{Cu} is reduced to less than ~ 15 nm, dislocation activities are greatly suppressed and their shielding effect is minimized, resulting in a significant reduction of deformability of the Cu layers (i.e. Cu layers become more brittle). Based on the above discussion, we chose h_{Cu} of 50 and 100 nm to be added to the monolithic Al–Mn/PI structure (samples B1, B2, and S) in order to optimize the ductility and the fracture properties of amorphous thin film on PI substrate.

Next, a fracture model proposed by Hsia et al. (1994) was employed to justify the effect of Cu layer thickness on the fracture behavior of B1 and B2 samples. In this model, crack propagation in a composite structure composed of submicron thick ductile and brittle layers is considered. This model considers the constraint effect of the ductile layer on the propagation of a crack initiated at the brittle layer and blocked by the interface. On the one hand, the dislocations emitted from the crack tip blunt the crack tip and consequently reduce the tensile stress at the crack tip. At the same time, these emitted dislocations also pile up at the interface sending back a stress to the crack tip, impeding further dislocation emission. Based on the crack tip shielding and blunting effects by the emitted dislocations, the equilibrium number of dislocations (n) is determined as (Hsia et al. 1994):

$$n = \frac{4\pi (1 - \upsilon)}{\ln \left(\frac{\tilde{h}}{\tilde{r}} \right)} \left(\frac{\tilde{K}_{app} \sqrt{\tilde{h}}}{A \sqrt{2\pi}} \sin\varphi \cos\frac{\varphi}{2} - \tilde{\gamma} \right), \quad (5)$$

where $\upsilon = 0.328$ is the Poisson's ratio of Cu (Yu and Spaepen 2004) and A is a factor that is slightly greater

than unity (Hsia et al. 1994). $\tilde{K}_{app}$, $\tilde{h}$, $\tilde{\gamma}$ and $\tilde{r}$ are the normalized values defined as:

$$\tilde{K}_{app} = \frac{K_{app}}{\mu \sqrt{\beta}}, \ \tilde{h} = \frac{h_\varphi}{b}, \ \tilde{\gamma} = \frac{\gamma}{\mu b}, \ \tilde{r} \approx 2.7 \frac{r_0}{b}, \quad (6)$$

where K_{app} is the far field stress intensity factor of the Cu thin film. The values of K_{app} are 0.97 and 1.17 MPa m$^{1/2}$ for the Cu layers in B1 and B2, respectively, calculated from Eqs. (1)–(3) (σ_{Cu} is thickness-dependent, taking the values of 1180 and 1000 MPa for the Cu layers in B1 and B2, respectively (Zhang et al. 2008); E_{Cu} is 90 GPa (Yu and Spaepen 2004); g_{Cu} (α, β) is 8.65 for both the Cu layers in B1 and B2 (Beuth Jr 1992). μ is the shear modulus of Cu, taking the value of 33.89 GPa (Yu and Spaepen 2004), $\beta = 2\sqrt{(2/\pi)}$ assuming that the crack has a semi-circular front, and $h_\varphi = h_{Cu}/(2\sin\varphi)$ being the maximum distance the leading dislocation can travel before it is blocked by the interface. φ is the angle that the slip plane inclines from the interface (φ is chosen as 45° without a loss of generality). b is the Burgers vector of Cu (2.56 Å). $\tilde{\gamma}$ is the normalized surface energy ($\tilde{\gamma} \approx 0.1684$ estimated from; Rice and Thomson 1974). r_0 is the effective core radius of dislocations ($r_0 = 1.725$ nm; Hsia et al. 1994). The equilibrium number of dislocations estimated from Eq. (5) is 22 and 28 for the Cu films in B1 and B2, respectively.

With the presence of the shielding effect of the dislocations, the stress intensity at the crack tip is defined as (Hsia et al. 1994):

$$K_{tip} = K_{app} - K_D, \quad (7)$$

where K_D is the contribution of the dislocations to the stress intensity at the crack tip (Hsia et al. 1994):

$$K_D = \frac{\mu b}{(1 - \upsilon)\sqrt{2\pi h_\varphi}} \frac{3}{2} \sin\varphi \cos\frac{\varphi}{2}. \quad (8)$$

The maximum tensile stress at the crack tip is determined as (Hsia et al. 1994):

$$\sigma_{tip} = \beta \frac{K_{tip}}{\sqrt{nb}}. \quad (9)$$

Using the input values described above, K_{tip} were estimated to be 0.92 and 1.13 MPa m$^{1/2}$, and σ_{tip} were estimated to be 1.94 and 2.12 GPa for samples B1 and B2, respectively. The higher value of the crack tip stress intensity (K_{tip}) in B2 shows that a thicker Cu layer can accommodate more damage and larger amounts of dislocations before fracture. These results are in agreement with our experimental observations

Fig. 5 SEM images of sample **a** M20, **b** B1, **c** B2 and **d** S at its respective critical strains. Uniaxial loading is applied in the horizontal direction in all samples as shown in (**a**). *White arrows* in (**a**) show the extensive shear bands formed, either inclined at an angle of $\sim 45°$ or perpendicular to the loading direction
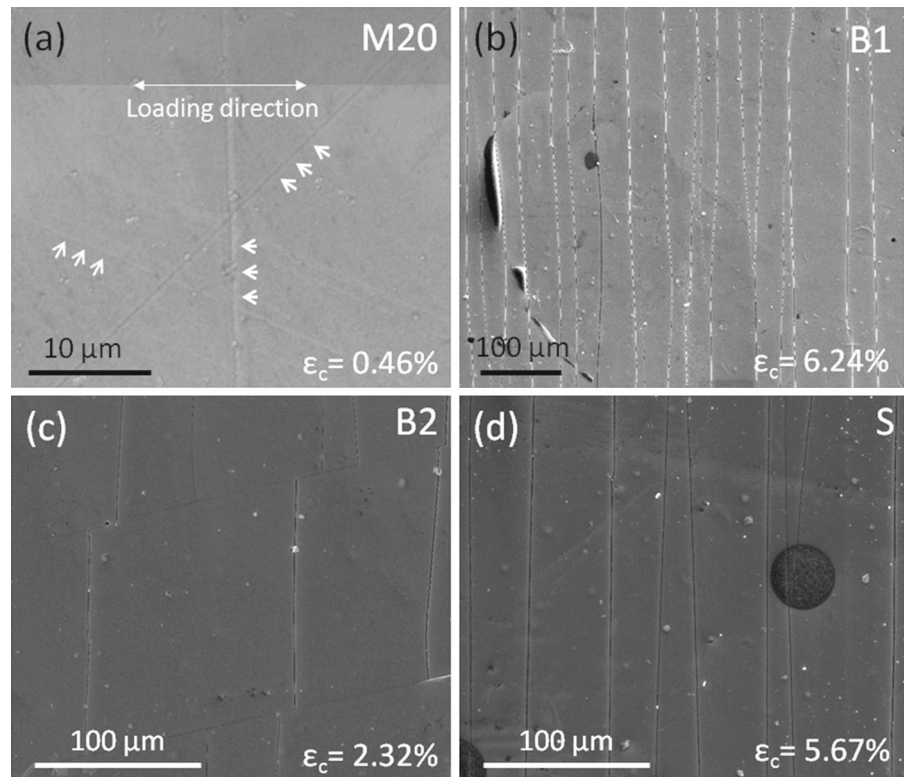
that the fracture toughness of the whole B2 sample is higher than B1 (Fig. 5d). Moreover, the fact that maximum tensile stress at the crack tip (σ_{tip}) in B2 is larger than that in B1 (along with the substrate effect as discussed later in Sect. 4.2) suggests that the Cu layer in sample B2 has a higher stress concentration than in B1, making the elongation of B2 smaller than B1, which agrees well with our experimental observations (Fig. 5a).

Finally, let's consider the behavior of the sandwiched trilayer sample S, which is the optimized solution that exhibits a combination of high ductility (5.67 %) and high fracture toughness (1.13 MPa m$^{1/2}$). Since cracking of nano-scaled multilayer films is initiated in the brittle layers and hindered by the ductile layers (Wu et al. 2014), in the cases of B1 and B2, the micro-cracks initiated at the top surface of the Al–Mn film and propagated to the Cu/Al–Mn interface. For sample S, having another Cu layer on the top will delay the crack initiation at the brittle Al–Mn layer, which eventually leads to the ductility enhancement. In this analysis, the effects of the brittle layer on the ductile layer contributing to the fracture mechanism were not

considered (Guo et al. 2015), and can be considered in future work.

4.2 Failure mechanisms at the film/polymer interface in multilayered samples

Together with the fracture mechanisms at the brittle/ductile interface, those at the film/polymer interface also contribute significantly to the fracture behavior of the multilayered samples. SEM image in Fig. 5b shows the surface of B1 at the critical strain. The presence of channeling cracks through the width without any shear bands confirmed the ductile fracture via the bilayer scheme (Was and Foecke 1996; Zhang et al. 2014). It is likely that the presence of a thin (50 nm) Cu layer dissipated the energy from the amorphous alloy layer to the PI substrate and thereby delayed the final failure (Chen et al. 2011a; Kou et al. 2014).

In sample S, the Cu layers limit the propagation of some shear bands distributing the plastic strain to many other bands, delaying fracture, which is why large plastic strain was observed. The failure mechanism can be

Fig. 6 **a**, **b** Cross-sectional ion beam images of the S sample at its critical strain. Image (**b**) was obtained after extensive ion etching of the crack in (**a**) to reveal the sandwich structure
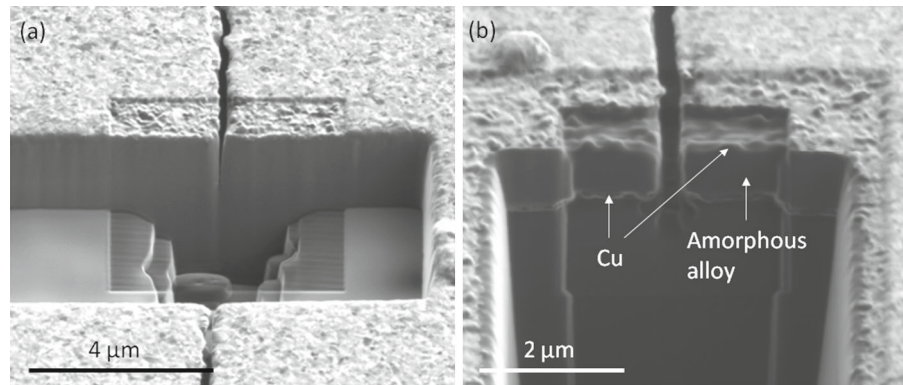
explained as follows. First, even with a thick (100 nm) Cu layer between the alloy and PI, which slows down the energy dissipation from the Cu layer to PI, sample S still possesses high ductility because of its hierarchical structure of the three layers. The three layers deform differently, i.e. the top surface Cu layer maintains/stabilizes ductility (of the Al–Mn layer) and together with the inner Cu layer they dissipate energy via their plasticity, preserving ductility and delaying the final failure of the whole structure (Chen et al. 2011a; Kou et al. 2014). Second, it was observed when running the DIC program that there were nearly no strain localizations on the sample S' surface. The idea of strain non-localization was first introduced to improve the ductility of nano-materials by designing three-layered stainless steel sheets with surface mechanical attrition treatments and co-rolling processes (Chen et al. 2008; Lu and Lu 2004). Strain non-localization mitigates the initiation of one critical major crack and delays the crack propagation by transferring the originally localized cracks to other positions (Kou et al. 2014). According to Lu et al. (2009), the critical condition for strain localization to take place is debonding between the film and the substrate, since debonding makes the film locally free-standing and thus necking of the film will be accommodated by local elongation. Figure 6 shows FIB images of the cross-section view of the tested S specimen and confirms that there was no debonding at the film/PI interface, and thereby no strain localization in the S samples. Since a strong bonding between the film and the PI substrate is very critical in maintaining high ductility for such systems, future work will be carried out to improve the adhesion of the film/polymer interface by tuning the surface roughness of the polymer substrate. Some related work has been done by

Table 2 Material properties used in the FEM model

| Material	E (GPa)	ν	σ_Y (MPa)	σ_f (MPa)
PI	2.5	0.34	69	–
M20	103.6	0.32	–	321.7
Cu	127	0.34	881.98	–

Properties of PI are from the manufacturer (Dupont 2004) and those of Cu thin film are from reference (Yu and Spaepen 2004), while the properties of the Al–Mn alloy layer are from experiments as listed in Table 1

others in references (Dauskardt et al. 1998; Lin and Liu 2008; Xu et al. 2011).

5 Finite element simulations

To provide further insight into the failure mechanism and to evaluate the interfacial fracture toughness of the film/PI systems under tensile loading, finite element simulations were performed using ANSYS (version 15). A two dimensional plane-strain model of the multilayered film on PI substrate under uniaxial tension was constructed, similar to that in Zhang and Li (2008). The total metallic film thickness h_T is 1.2 µm and the PI substrate thickness is 7.6 µm. The length l of the film/substrate system was set at 3.12 µm. The material properties used in the finite element method (FEM) model are listed in Table 2. The stress-strain curve of PI is obtained from the manufacturer specifications (Dupont 2004) and that of Cu thin film is from Ref. Yu and Spaepen (2004). The properties of the Al–Mn alloy layer were obtained from experiments, as listed in Table 1. With the implementation of the cohesive zone model (Park and Paulino 2013) in Ansys APDL, the

Fig. 7 Elastic strain energy density distributions of sample. **a** M20 and **b** S at a strain of 0.46%
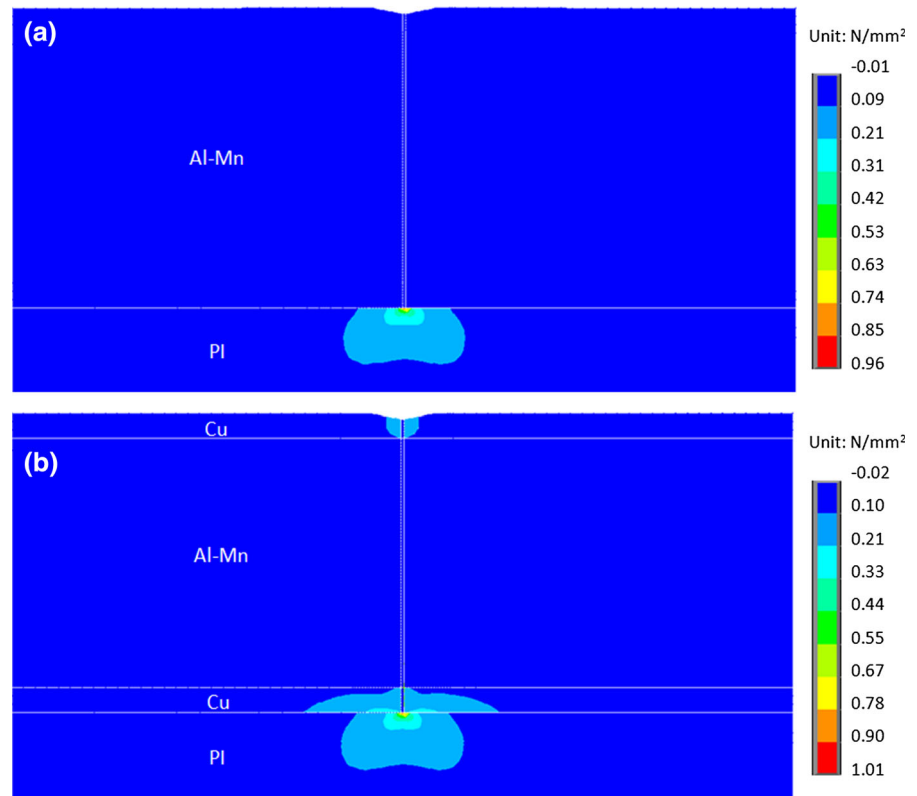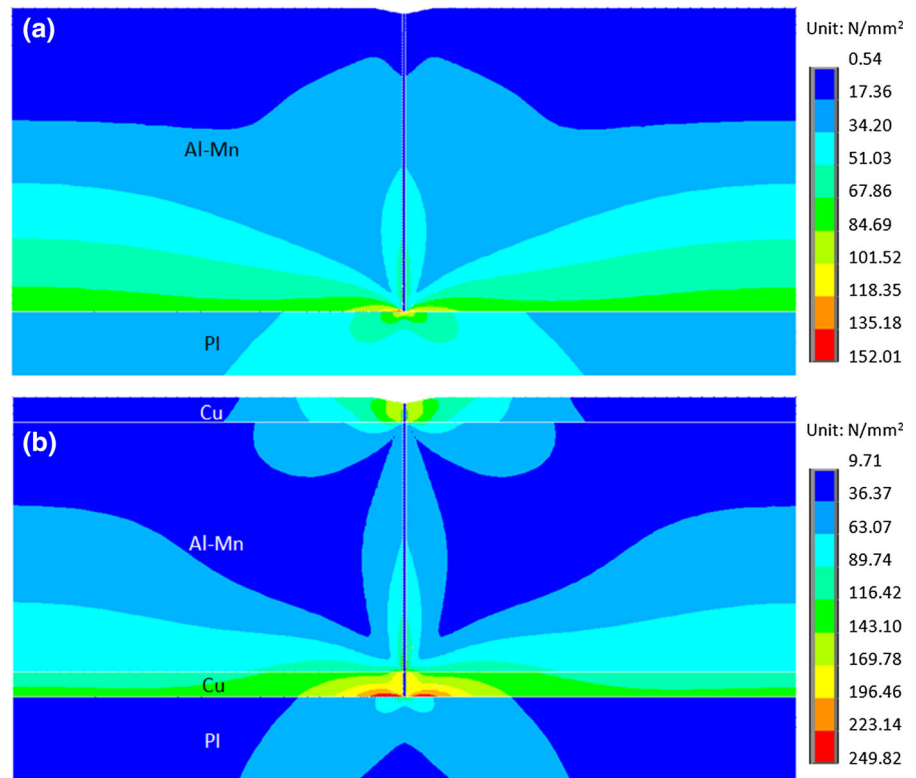

strain energy density distribution, von Mises equivalent stress distribution and J-integral (which represents interfacial adhesion toughness) were obtained.

Cohesive zone models were defined at both the film itself and the interface between the film and the PI substrate. Exponential law was selected as the cohesive law, which describes mathematically the separation or debonding of two parts of the film and of two material surfaces (Park and Paulino 2013). The stress for which the crack opening starts was assumed to be equal to the yield stress or the fracture stress of the material considered (Dugdale 1960), i.e. Cu and Al–Mn alloy. The maximum normal traction for which the film/substrate interface starts to debond was assumed to be equal to the yield stress or fracture stress of the material that adheres to the PI substrate (Xu et al. 2010). Normal separation across the interface and the shear separation, where the maximum normal traction is attained, were assumed to be identical and obey the law of the fracture energy represented in Xu et al. (2010). To introduce an imperfection where the crack can nucleate, a V-shaped notch $0.2h_T$ wide and $0.02h_T$ deep was placed at the top of the film (Li and Suo 2007; Lu et al. 2010;

Zhang and Li 2008). Both the film and the substrate were meshed by the two-dimensional 8-node structural solid elements Plane183 with the plane strain option. The interfaces were meshed by the 6-node cohesive elements Inter203. The vertical displacement along the bottom of the substrate as well as the horizontal displacement along the centerline of the system was set to zero, whereas a uniform horizontal displacement of $u/2$ was applied to both sides of the film/substrate system. The nominal strain of the system is then u/l, where l denotes the length of the film/substrate system. Finally, convergence analysis was performed to get the optimal mesh.

To investigate the adhesion of the interface between two dissimilar, non-linear elastic materials (i.e. the film/PI system), path-independent J-integral has been proven to be the only feasible computational method (Anderson 2005; Rice and Sih 1965; Tran et al. 2013). A strain of 0.46% (i.e. critical strain of the sample M20) was applied to all multilayer samples. Twelve contours were defined around the crack tip, which rested at the film/substrate interface, to calculate the converged J-integral values. Figure 7 shows the elastic strain energy

Fig. 8 Von Mises equivalent stress distributions of sample. **a** M20 and **b** S at a strain of 0.46%

density distributions of the M20 and S samples at 0.46% strain. It can be seen that the presence of a Cu layer sustained a high amount of strain energy. This confirms that the two Cu layers dissipate energy via their plasticity, together with the ductility of the polymer substrate, preserving the ductility and then delaying the final failure of the whole metallic system (Chen et al. 2011a; Kou et al. 2014). Figure 8 shows the von Mises equivalent stress distributions of M20 and S. The two Cu layers sustain much of the stress distributed to the whole film, which obviously reduces the stress that the alloy layer has to endure. This makes the elongation of the sample S larger and the alloy layer can possess higher critical stress at its critical strain. The J-integrals of the film/substrate interface at the same strain of 0.46% (Fig. 9) show that the adhesion of the interface increases significantly with the added Cu layers (from 0.34 J/m^2 for M20 to 0.45 J/m^2 for B2 and S). This result confirms that the bonding between the film and the substrate was improved, making it a critical condition for strain non-localization, delaying the crack propagation by transferring the originally local-
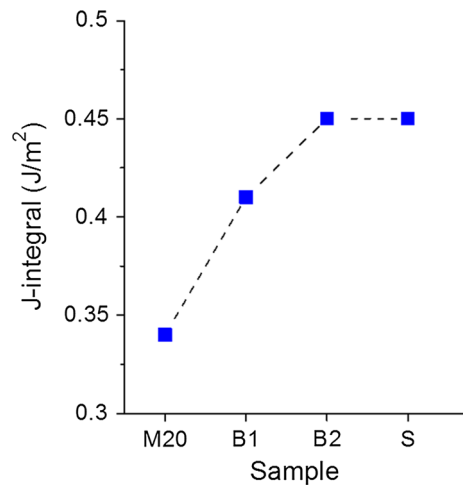
Fig. 9 J-integrals of the film/substrate interface at the applied strain of 0.46%

ized cracks to other positions (Kou et al. 2014; Lu et al. 2009).

Finally, to evaluate the ability of the multilayered film/PI systems to resist delamination at the
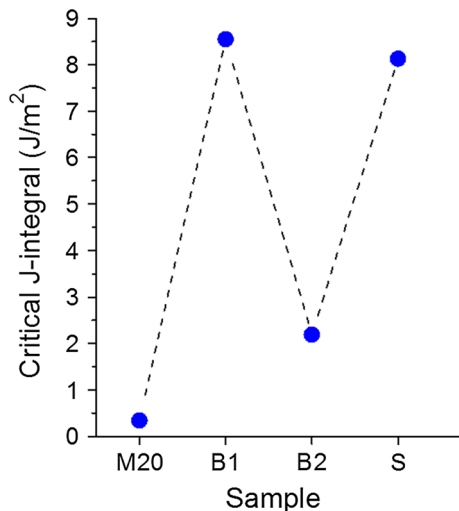
Fig. 10 Critical J-integrals of the film/substrate interface of the sample M20, B1. B2 and S at their critical strains of 0.46, 6.24, 2.32 and 5.67%, respectively

film/polymer interface, interfacial fracture toughness (i.e. critical J-integrals) of all samples were calculated (Tran et al. 2013). Samples M20, B1, B2 and S were applied with their experimental critical strains of 0.46, 6.24, 2.32 and 5.67%, respectively (Fig. 4a). The results in Fig. 10 show that with the sandwiching scheme, the interfacial fracture toughness can be enhanced twenty four times from 0.34 J/m^2 (sample M20) to 8.13 J/m^2 (sample S). This result again confirms the significant improvement of the adhesion between the film and the substrate via the sandwich structure.

6 Conclusions

Mechanical properties of monolithic and multilayered Al–Mn thin films coated on PI substrates were studied by tensile testing and finite element methods. Among the monolithic films, the amorphous Al–Mn possesses the highest fracture toughness, but limited ductility and poor resistance to interfacial delamination. To improve the stretchability of the system without compromising the fracture toughness, bilayered and trilayered films were designed by adding Cu buffer layers to the system. It was found that the bilayered structure with 50 nm Cu buffer layer improves the ductility of amorphous Al–Mn by more than ten times while the trilayered structure optimizes both ductility and fracture toughness. Analytical modeling and finite element analysis show

that in the trilayered structure, the topmost Cu layer retards crack initiation, while the inner Cu layer dissipates strain energy and improves film/PI adhesion. In this case, the elongation was enhanced more than ten times and the interfacial fracture toughness twenty four times with a limited sacrifice of fracture toughness (less than 18%). The results of this work thus provide important guidelines for optimizing mechanical properties of future flexible electronics, whose performance requires reasonable ductility of crystalline and amorphous metallic films on polymer substrates.

References

Anderson PM, Li C (1993) Crack-dislocation modeling of ductile-to-brittle. MRS Proc 308:731–736

Anderson TL (2005) Fracture mechanics: fundamentals and applications. CRC Press, Boca Raton

Beuth JL Jr (1992) Cracking of thin bonded films in residual tension. Int J Solids Struct 29:1657–1675

Bonderover E, Wagner S (2004) A woven inverter circuit for e-textile applications. IEEE Electr Dev L 25:295–297

Brabec CJ (2004) Organic photovoltaics: technology and market. Sol Energy Mat Sol C 83:273–292

Cardarelli F (2008) Materials handbook: a concise desktop reference. Springer, London

Chen AY, Li DF, Zhang JB, Song HW, Lu J (2008) Make nanostructured metal exceptionally tough by introducing non-localized fracture behaviors. Scr Mater 59:579–582

Chen AY, Ruan HH, Zhang JB, Liu XR, Lu J (2011a) Introducing a hierarchical structure for fabrication of a high performance steel. Mater Chem Phys 129:1096–1103

Chen W, Chan KC, Guo SF, Yu P (2011b) Plasticity improvement of an Fe-based bulk metallic glass by geometric confinement. Mater Lett 65:1172–1175

Chu CW, Jang JSC, Chiu SM, Chu JP (2009) Study of the characteristics and corrosion behavior for the Zr-based metallic glass thin film fabricated by pulse magnetron sputtering process. Thin Solid Films 517:4930–4933

Chu JP, Huang JC, Jang JSC, Wang YC, Liaw PK (2010) Thin film metallic glasses: preparations, properties, and applications. JOM 62:19–24

Cordill MJ, Taylor A, Schalko J, Dehm G (2010) Fracture and delamination of chromium thin films on polymer substrates. Metall Mater Trans A 41A:870–875

Dauskardt RH, Lane M, Ma Q, Krishna N (1998) Adhesion and debonding of multi-layer thin film structures. Eng Fract Mech 61:141–162

Dugdale DS (1960) Yielding of steel sheets containing slits. J Mech Phys Solids 8:100–104

Dupont (2004) Physical and thermal properties of kapton® polyimide films. http://www.dupont.com/content/dam/assets/products-and-services/membranes-films/assets/DEC-Kapton-summary-of-propertiespdf

Eberl C (2010) Digital image correlation and tracking. Matlab center. https://www.mathworks.com/matlabcentral/profile/authors/502139-christoph-eberl

Frank S, Gruber PA, Handge UA, Spolenak R (2011) In situ studies on the cohesive properties of alpha- and beta-Ta layers on polyimide substrates. Acta Mater 59:5881–5892

Frank S, Handge UA, Olliges S, Spolenak R (2009) The relationship between thin film fragmentation and buckle formation: synchrotron-based in situ studies and two-dimensional stress analysis. Acta Mater 57:1442–1453

Freund LB, Suresh S (2003) Thin film materials: stress, defect formation, and surface evolution. Cambridge University Press, Cambridge

George M, Coupeau C, Colin J, Grilhe J (2005) Mechanical behaviour of metallic thin films on polymeric substrates and the effect of ion beam assistance on crack propagation. Acta Mater 53:411–417

Guo T, Qiao L, Pang X, Volinsky AA (2015) Brittle film-induced cracking of ductile substrates. Acta Mater 99:273–280

Hofmann DC, Suh J-Y, Wiest A, Duan G, Lind M-L, Demetriou MD, Johnson WL (2008) Designing metallic glass matrix composites with high toughness and tensile ductility. Nature 451:1085–1089

Hsia KJ, Suo Z, Yang W (1994) Cleavage due to dislocation confinement in layered materials. J Mech Phys Solids 42:877–896

Huang R, Prévost JH, Huang ZY, Suo Z (2003) Channel-cracking of thin films with the extended finite element method. Eng Fract Mech 70:2513–2526

Inoue A (2001) Bulk amorphous and nanocrystalline alloys with high functional properties. Mater Sci and Eng A 304–306:1–10

Kou H, Lu J, Li Y (2014) High-strength and high-ductility nanostructured and amorphous metallic materials. Adv Mater 26:5518–5524

Li T, Suo Z (2007) Ductility of thin metal films on polymer substrates modulated by interfacial adhesion. Int J Solids Struct 44:1696–1705

Li XF, Zhang KF, Wang GF (2007) Preparation and tensile properties of amorphous Fe78Si9B13/nano-Ni laminated composite. Mater Lett 61:4901–4905

Lin YS, Liu HM (2008) Enhanced adhesion of plasma-sputtered copper films on polyimide substrates by oxygen glow discharge for microelectronics. Thin Solid Films 516:1773–1780

Lu K, Lu J (2004) Nanostructured surface layer on metallic materials induced by surface mechanical attrition treatment. Mater Sci Eng A 375–377:38–45

Lu N, Suo Z, Vlassak JJ (2010) The effect of film thickness on the failure strain of polymer-supported metal films. Acta Mater 58:1679–1687

Lu N, Wang X, Suo Z, Vlassak J (2007) Metal films on polymer substrates stretched beyond 50%. Appl Phys Lett 91:221909

Lu N, Wang X, Suo Z, Vlassak J (2009) Failure by simultaneous grain growth, strain localization, and interface debonding in metal films on polymer substrates. J Mater Res 24:379–385

Lumelsky VJ, Shur MS, Wagner S (2001) Sensitive skin. IEEE Sens J 1:41–51

Macionczyk F, Brückner W (1999) Tensile testing of AlCu thin films on polyimide foils. J Appl Phys 86:4922–4929

McHenry ME, Willard MA, Laughlin DE (1999) Amorphous and nanocrystalline materials for applications as soft magnets. Prog Mater Sci 44:291–433

Misra A, Hirth JP, Hoagland RG (2005) Length-scale-dependent deformation mechanisms in incoherent metallic multilayered composites. Acta Mater 53:4817–4824

Moffat TP, Stafford GR, Hall DE (1993) Pitting corrosion of electrodeposited aluminum–manganese alloys. J Electrochem Soc 140:2779–2786

Nieh TG, Barbee TW, Wadsworth J (1999) Tensile properties of a free-standing Cu/Zr nanolaminate (or compositionally-modulated thin film). Scr Mater 41:929–935

Niu RM, Liu G, Wang C, Zhang G, Ding XD, Sun J (2007) Thickness dependent critical strain in submicron Cu films adherent to polymer substrate. Appl Phys Lett 90:161907

Pan B, Qian K, Xie H, Asundi A (2009) Two-dimensional digital image correlation for in-plane displacement and strain measurement: a review. Meas Sci Technol 20:062001

Park K, Paulino GH (2013) Cohesive zone models: a critical review of traction-separation relationships across fracture surfaces. Appl Mech Rev 64:060802–060802

Pei HJ, Lee CJ, Du XH, Chang YC, Huang JC (2011) Tension behavior of metallic glass coating on Cu foil. Mater Sci Eng A 528:7317–7322

Phan MH, Peng HX (2008) Giant magnetoimpedance materials: fundamentals and applications. Prog Mater Sci 53:323–420

Rice JR, Sih GC (1965) Plane problems of cracks in dissimilar media. J Appl Mech 32:418–423

Rice JR, Thomson R (1974) Ductile versus brittle behaviour of crystals. Philos Mag 29:73–97

Ritchie RO (2011) The conflicts between strength and toughness. Nat Mater 10:817–822

Ruan SY, Schuh CA (2009) Electrodeposited Al–Mn alloys with microcrystalline, nanocrystalline, amorphous and nano-quasicrystalline structures. Acta Mater 57:3810–3822

Schuh CA, Hufnagel TC, Ramamurty U (2007) Mechanical behavior of amorphous alloys. Acta Mater 55:4067–4109

Tran HT, Shirangi MH, Pang X, Volinsky AA (2013) Temperature, moisture and mode-mixity effects on copper leadframe/EMC interfacial fracture toughness. Int J Fract 185:115–127

Varias AG, Suo Z, Shih CF (1991) Ductile failure of a constrained metal foil. J Mech Phys Solids 39:963–986

Wagner S, Lacour SP, Jones J, P-hI Hsu, Sturm JC, Li T, Suo Z (2004) Electronic skin: architecture and components. Phys E 25:326–334

Wang J, Anderson PM (2005) Pinch-off maps for the design of morphologically stable multilayer thin films with immiscible phases. Acta Mater 53:5089–5099

Wang WH (2009) Bulk metallic glasses with functional physical properties. Adv Mater 21:4524–4544

Was GS, Foecke T (1996) Deformation and fracture in micro-laminates. Thin Solid Films 286:1–31

Wu K, Zhang JY, Zhang P, Wang YQ, Liu G, Zhang GJ, Sun J (2014) Fracture behavior and adhesion energy of nanostructured Cu/Mo multilayer films. Mater Sci Eng A 613:130–135

Xiang Y, Li T, Suo ZG, Vlassak JJ (2005) High ductility of a metal film adherent on a polymer substrate. Appl Phys Lett 87:161910

Xu W, Lu TJ, Wang F (2010) Effects of interfacial properties on the ductility of polymer-supported metal films for flexible electronics. Int J Solids Struct 47:1830–1837

Xu W, Yang JS, Lu TJ (2011) Ductility of thin copper films on rough polymer substrates. Mat Des 32:154–161

Yu DYW, Spaepen F (2004) The yield strength of thin copper films on Kapton. J Appl Phys 95:2991–2997

Zhang JY, Liu G, Sun J (2014) Self-toughening crystalline Cu/amorphous Cu–Zr nanolaminates: deformation-induced devitrification. Acta Mater 66:22–31

Zhang JY et al (2011) Length-scale-dependent deformation and fracture behavior of Cu/X multilayers: the constraining effects of the ductile phase on the brittle phase. Acta Mater 59:7368–7379

Zhang Z, Li T (2008) Effects of grain boundary adhesion and grain size on ductility of thin metal films on polymer substrates. Scr Mater 59:862–865